# Observational Constraints of Radial Migration in the Galactic Disk Driven by the Slowing Bar

HanYuan Zhang[1] , Vasily Belokurov[1] , N. Wyn Evans[1] , Jason L. Sanders[2] , Yuxi(Lucy) Lu[3,4] , Chengye Cao[5] ,
GyuChul Myeong[1] , Adam M. Dillamore[2] , Sarah G. Kane[1] , and Zhao-Yu Li[5,6]

[1] Institute of Astronomy, University of Cambridge, Madingley Rd., Cambridge CB3 0HA, UK; hz420@cam.ac.uk
[2] Department of Physics and Astronomy, University College London, London WC1E 6BT, UK
[3] Department of Astronomy, The Ohio State University, Columbus, 140 W. 18th Ave., OH 43210, USA
[4] Center for Cosmology and Astroparticle Physics (CCAPP), The Ohio State University, 191 W. Woodruff Ave., Columbus, OH 43210, USA
[5] Department of Astronomy, School of Physics and Astronomy, 800 Dongchuan Rd., Shanghai Jiao Tong University, Shanghai 200240, People's Republic of China
[6] National Key Laboratory of Dark Matter Physics, School of Physics and Astronomy, Shanghai Jiao Tong University, Shanghai 200240, People's Republic of China

## Abstract

Radial migration is an important dynamical effect that has reshaped the Galactic disk, but its origin has yet to be elucidated. In this work, we present evidence that resonant dragging by the corotation of a decelerating bar could be the main driver of radial migration in the Milky Way disk. Using a test particle simulation, we demonstrate this scenario explains the two distinct age–metallicity sequences observed in the solar vicinity: the plateauing upper sequence is interpreted as stars dragged outward by the expanding corotation of the decelerating bar and the steeper lower sequence as stars formed locally around the solar circle. The upper migrated sequence dominates at guiding radii around the current corotation radius of the bar, $R \sim 7$ kpc, but rapidly dies away beyond this where the mechanism cannot operate. This behavior naturally explains the radial dependence of the $[\alpha/\mathrm{Fe}]$-bimodality, in particular the truncation of the high-$[\alpha/\mathrm{Fe}]$ disk beyond the solar circle. Under our proposed radial migration scenario, we constrain the Milky Way bar's pattern speed evolution using the age–metallicity distribution of stars currently trapped at corotation. We find the bar likely formed with an initial pattern speed of $60-100$ km s$^{-1}$ kpc$^{-1}$ and began decelerating $6-8$ Gyr ago at a rate of $-\dot{\Omega}/\Omega^2 \sim 0.0025 - 0.0040$ (where the quoted ranges include systematic uncertainties).

Unified Astronomy Thesaurus concepts: Milky Way dynamics (1051); Galactic bar (2365); Milky Way evolution (1052); Milky Way disk (1050); Galaxy evolution (594)

## 1. Introduction

Stars in the galactic disk can be scattered from their presumed near-circular birth orbits to their present-day orbits by secular processes or external perturbations. This change in stellar orbits can be decomposed into two different components, the drifting of the angular momentum ($\Delta L_z$, dubbed "radial migration," J. A. Sellwood & J. J. Binney 2002, or "churning," R. Schönrich & J. Binney 2009) and the amplification in the radial oscillation or the radial action ($\Delta J_r$, dubbed "radial heating" or "blurring").

Many studies have shown that radial migration in the Milky Way disk is strong using the age and metallicity of various kinds of tracers (e.g., R. Schönrich & J. Binney 2009; J. L. Sanders & J. Binney 2015; N. Frankel et al. 2018; L. Beraldo e Silva et al. 2021; H. Zhang et al. 2021; J. Lian et al. 2022a; M. Haywood et al. 2024). The age and metallicity of stars are important in understanding the migration history of the Galactic disk because they encode the birth radii of stars (J. A. Sellwood & J. J. Binney 2002; I. Minchev et al. 2018; Y. L. Lu et al. 2024; B. Ratcliffe et al. 2024a). N. Frankel et al. (2020) quantified the strength of radial migration and heating in the Galactic disk and showed that radial migration in the Galactic disk is significantly more efficient than radial heating. Results from analytic studies and simulations have shown that

radial migration could reshape the chemical properties of the Galactic disk, such as the azimuthal abundance distribution of stars (P. Di Matteo et al. 2013), the $[\alpha/\mathrm{Fe}]$-bimodality of the disk (S. Sharma et al. 2021a), and the age–metallicity distribution (M. Haywood et al. 2024). Therefore, it is important to understand better the driving mechanisms of radial migration to unveil the evolution of the Galactic disk.

Theoretical analysis and $N$-body simulations have shown that transient spiral arms can drive efficient radial migration of stars (J. A. Sellwood & J. J. Binney 2002; R. Roškar et al. 2008, 2012), and many studies have emphasized the importance of evolving spiral arms and bar–spiral resonance overlap (I. Minchev & A. C. Quillen 2006; I. Minchev & B. Famaey 2010; I. Minchev et al. 2011; M. Solway et al. 2012; K. J. Daniel et al. 2019, and references therein). Giant molecular clouds and satellite galaxies also cause orbital scattering (A. C. Quillen et al. 2009; R. Schönrich & J. Binney 2009; C. Carr et al. 2022). C. Hamilton et al. (2024) recently argued that using spiral arms to produce the required relative coldness of the migration process observed in the Galactic disk (N. Frankel et al. 2020) is challenging, partly because resonance overlap also heats stars during transportation. In response, J. A. Sellwood & J. Binney (2025) provided evidence that the heating may have been overestimated by C. Hamilton et al. (2024) in their idealized simulations. Another important potential source of radial migration is the slowing of the Galactic bar. During deceleration, the orbital resonances of the bar (e.g., corotation and outer Lindblad) move outward through the disk, trapping stars and dragging them outward

(R. Chiba & R. Schönrich 2021; R. Chiba et al. 2021). This mechanism has been demonstrated in *N*-body simulated galaxies as an efficient way to transport stars (A. Halle et al. 2015, 2018; S. Khoperskov et al. 2020; M. Haywood et al. 2024). Crucially, S. Khoperskov et al. (2020) showed that stars transported with the corotation resonance of the bar had near-circular orbits when they left the corotation resonance (see also R. Chiba et al. 2021) meaning resonant dragging has exactly the required properties of the radial migration mechanism.

A key parameter of the Galactic bar is its angular frequency, or pattern speed $\Omega$. Past observations have constrained the pattern speed of the Galactic bar to $\sim$34–41 km s$^{-1}$ kpc$^{-1}$ (M. Portail et al. 2017; J. Bovy et al. 2019; J. L. Sanders et al. 2019; J. Binney 2020; R. Chiba & R. Schönrich 2021; D. Kawata et al. 2021), and more recently, to $\sim$32–35 km s$^{-1}$ kpc$^{-1}$ (J. P. Clarke & O. Gerhard 2022; A. M. Dillamore et al. 2024a; H. Zhang et al. 2024b). This puts the corotation radius of the Galactic bar at $R \sim 6.5$–7.5 kpc given that the rotation velocity of the disk is 230–240 km s$^{-1}$ (P. J. McMillan 2017). However, in the past, the Galactic bar may not have been rotating with the pattern speed we measure today. It has been demonstrated analytically and computationally that the Galactic bar could decelerate due to dynamical friction against the dark matter halo (V. P. Debattista & J. A. Sellwood 2000; E. Athanassoula 2003; M. D. Weinberg & N. Katz 2007, and references therein). R. Chiba et al. (2021) and R. Chiba & R. Schönrich (2021) used the kinematics and chemistry of the solar neighborhood stars to constrain the deceleration rate of the Milky Way bar to $\eta = -\dot{\Omega}/\Omega^2 \sim 0.0025 - 0.0045$. A slowing bar has been shown to be crucial in Milky Way modeling (R. Chiba et al. 2021; A. M. Dillamore et al. 2024b; C. Li et al. 2024; Z. Yuan et al. 2024). In addition, the slowdown rate of the bar is an important tracer of the kinematics of the dark matter halo (E. Athanassoula 2003), which opens a new window to constrain the nature of dark matter.

In this work, we compare the age–metallicity plane observed in the solar vicinity (M. Xiang & H.-W. Rix 2022) to a test particle simulation with a decelerating bar and investigate how bar-driven radial migration affects the age–metallicity plane in the solar vicinity. We describe the data and quality cuts that we adopt in Section 2. We present the setup of the test particle simulation in Section 3. In Section 4, we compare the age–metallicity plane of the test particle simulation to the observation (Section 4.1), we discuss the implications of this radial migration mechanism to the disk [$\alpha$/Fe]-bimodality (Section 4.2), and we infer the pattern speed evolution history of the Milky Way bar (Section 4.3). In Section 5, we discuss other implications and other predictions that we expect to observe in the Milky Way under the bar-driven radial migration scenario.

## 2. Data

We use the stellar parameter and isochrone age measurements of $\sim$247,000 subgiant stars derived from LAMOST DR7 spectra by M. Xiang et al. (2019) and M. Xiang & H.-W. Rix (2022). The typical age uncertainty is $\sim$7.5% for stars younger than 10 Gyr and $\sim$10% for older stars. To obtain the stellar kinematics, we use the astrometric measurements from Gaia DR3 (Gaia Collaboration et al. 2023), the geometric distances derived in C. A. L. Bailer-Jones et al. (2021), and the line-of-sight velocity measurements from LAMOST (L.-C. Deng et al. 2012). We calculate the orbital parameters (e.g., eccentricity and guiding radius) of stars using the Milky Way potential in

P. J. McMillan (2017) using AGAMA (E. Vasiliev 2019). To ensure reliable orbital parameters, we select stars with small parallax uncertainties and small radial velocity uncertainties, i.e., $\varpi/\sigma_{\varpi} > 5$ and $\sigma_{v_{\rm los}} < 10$ km s$^{-1}$. We remove stars with metallicity error $\sigma_{\rm [Fe/H]} > 0.1$ or age error $\sigma_{\tau} > 1$ Gyr. To select stars belonging to the Galactic disk, we keep stars with orbital eccentricity $< 0.5$, vertical height $|z| < 1$ kpc, [Fe/H] $> -1$, and $\tau < 11.5$ Gyr. These values are consistent with the metallicity and age measurements of the spin-up epoch of the Milky Way (A. Miglio et al. 2021; V. Belokurov & A. Kravtsov 2022, 2024; C. Conroy et al. 2022; H.-W. Rix et al. 2022; A. B. A. Queiroz et al. 2023; V. Chandra et al. 2024; X. Liao et al. 2024; H. Zhang et al. 2024a, 2024c). There are $\sim$128,000 stars left after these selections and $\sim$97% of them reside within 2.5 kpc of the Sun.

## 3. Simulation

We run a test particle simulation with a realistic Galactic potential. We gradually release particles into the simulation to investigate the response of stars of different ages to a decelerating bar. We summarize the key information here and present the details in Appendix A.

We set up a time-evolving Galactic potential using a similar approach to that of A. M. Dillamore et al. (2024a). To ensure the realism of the simulation, we adopt the potential of the inner Galaxy from M. Portail et al. (2017) and M. C. Sormani et al. (2022). We grow the Galactic bar 4 Gyr into the simulation, increasing the Galactic bar strength following the prescription in W. Dehnen (2000). We let the bar reach its maximum strength at $t_{\rm bf} = 5$ Gyr and slow the bar pattern speed after this. We set the initial pattern speed to 80 km s$^{-1}$ kpc$^{-1}$ and adopt a constant slowdown rate $\eta = -\dot{\Omega}/\Omega^2 = 0.003$. We also adjust the bar length according to the pattern speed to ensure $R_{\rm CR}/R_{\rm bar}$ is constant as the bar length should increase during deceleration (E. Athanassoula 1992). At the final time of 11.5 Gyr, the pattern speed is $\sim$34 km s$^{-1}$ kpc$^{-1}$, similar to the measurements of the Milky Way bar (J. P. Clarke & O. Gerhard 2022; H. Zhang et al. 2024b), with corotation radius at $R_{\rm CR} \sim 6.8$ kpc. The exact pattern speed evolution is described in Appendix A.

We initialize the phase space of the test particles using the quasi-isothermal disk model (J. Binney 2010). We linearly increase the scale length of the disk model from 1 to 3.5 kpc during the simulation to mimic inside-out disk formation. The details of the initial phase space distribution of the generated test particles are described in Appendix A. Every 100 Myr, we sample 10,000 particles from the disk model and add them to the simulation. To simulate dynamical heating, we also give random velocity kicks to the stars by convolving their three Cartesian velocity components with an isotropic Gaussian distribution, $\mathcal{N}(1, 0.03)$, every 100 Myr. The resulting age–velocity dispersion relation is roughly consistent with Milky Way observations (S. Sharma et al. 2021b). We assign a metallicity to each particle according to its birth radius and age using the method described in Y. L. Lu et al. (2024) to better compare observation and simulation. To mimic the spatial coverage of the data, we apply a simple spatial cut to the output of the test particle simulation. We place the Sun at $R_{\odot} = 8.2$ kpc from the Galactic center (J. Bland-Hawthorn & O. Gerhard 2016) and at an angle of $-25°$ relative to the orientation of the Galactic bar (J. Bovy et al. 2019). Particles beyond 2.5 kpc from the Sun are removed. We use this
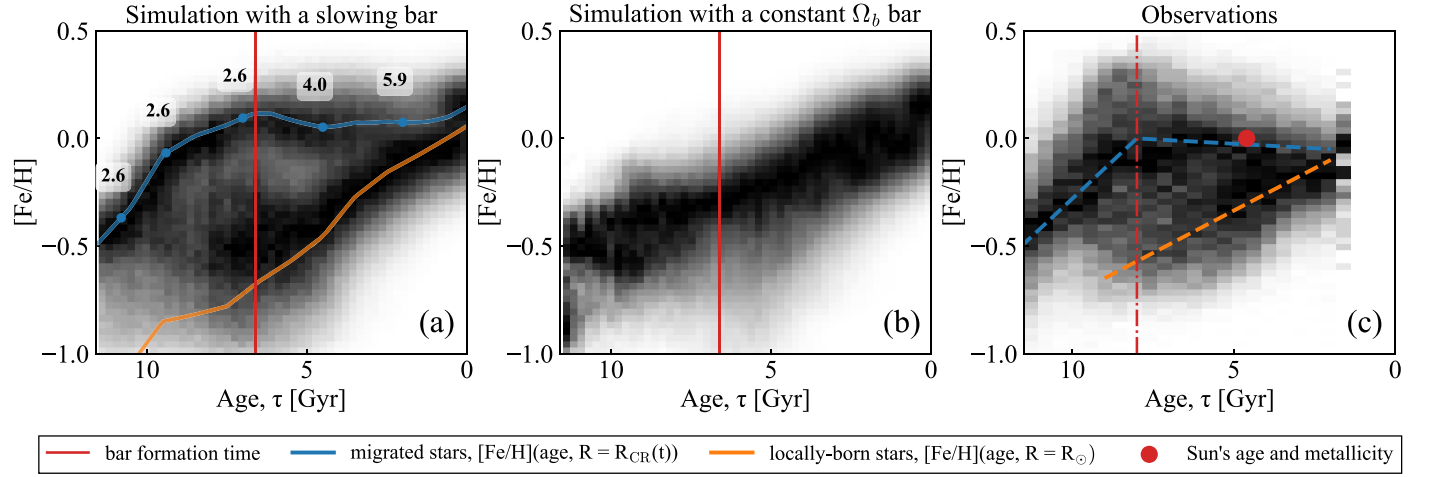
**Figure 1.** Left panel (a): the age–metallicity plane of the test particle simulation with a slowing-down bar. The blue line shows the metallicity evolution for stars that formed at the corotation radius of their corresponding age, $[\mathrm{Fe/H}](\tau, R_{\mathrm{CR}}(\tau))$, where the blue dots and annotation denote $R_{\mathrm{CR}}(t)$ at the respective times in units of kiloparsecs; the orange line shows the metallicity evolution of stars that formed around the solar circle, $[\mathrm{Fe/H}](\tau, R_{\odot})$. The red line indicates the moment of bar formation, $t_{\mathrm{bf}}$. Middle panel (b): the same as panel (a), except that the Galactic bar is rotating with a constant pattern speed at all times. Right panel (c): the column-normalized age–metallicity distribution of the subgiant-star sample we constructed based on M. Xiang & H.-W. Rix (2022), where the red circle indicates the Sun in this plane. The blue and orange dashed lines denote the upper and lower age–metallicity sequences, and the red dashed–dotted line marks the turning point of the upper sequence.

subsample of simulated test particles in the following sections unless otherwise stated.

## 4. Results

In this section, we analyze the results of the test particles and compare them to the observations in the solar vicinity.

### 4.1. Age–Metallicity Sequences in the Solar Vicinity

Panel (a) of Figure 1 shows the column-normalized age–metallicity distribution of the simulated particles in the solar vicinity. Two clear sequences are apparent: an upper sequence that rises rapidly at early times and flattens for stars formed since the bar began decelerating (marked by the red solid line), and a lower sequence that exhibits a strong age–metallicity correlation all the way to young ages. We identify the two sequences with migrated and local stars, respectively. The orange solid line, $[\mathrm{Fe/H}](t, R_{\odot})$, represents the evolution of metallicity for particles that formed at the present solar radius, $R_{\odot}$, demonstrating that the local sequence is composed of stars born around the solar circle.

The migrated sequence is for particles that formed inside the solar circle and were dragged to the solar vicinity by the bar corotation resonance. The resonant dragging by the corotation of a decelerating bar increases the angular momentum of the trapped stars (R. Chiba et al. 2021), forcing them to migrate with the expansion of the corotation radius. This migration mechanism has also been identified in many N-body simulated galaxies (A. Halle et al. 2015, 2018; S. Khoperskov et al. 2020). For particles seeded before the bar formation, those that formed and reside around the initial corotation radius ($R_{\mathrm{CR,0}} = 2.6$ kpc in the simulation) are trapped at the moment of bar formation and are dragged later by the expansion of the corotation radius. This corresponds to the portion of the migrated sequence with a quick metallicity increase as a function of age. During bar deceleration, the corotation resonance expands and sweeps through the disk. The corotation resonance then traps particles born at larger radii, which have lower metallicity at the same age, causing the flattening in the

age–metallicity sequence after bar formation. We use the blue solid line to denote the metallicity evolution for particles formed at the corotation radius at their birth time $R_{\mathrm{CR}}(t)$, i.e., $[\mathrm{Fe/H}](t, R_{\mathrm{CR}}(t))$, where

$$R_{\mathrm{CR}}(t) = \begin{cases} R_{\mathrm{CR,0}}, & t < t_{\mathrm{bf}} \\ V_c/\Omega(t), & t > t_{\mathrm{bf}}. \end{cases} \tag{1}$$

To summarize, the migrated sequence is composed of the age–metallicity relation at the initial corotation radius for the time before the bar formation and the segments of the age–metallicity relation at the corresponding corotation radii at later times. The migrated sequence after the bar formation is flatter than the expected age–metallicity sequence at a fixed radius because stars at larger radii are dragged, but the extent of flattening depends on the details of the chemical evolution history (see Figure A1 and Section 4.3.1 for clarification).

As a comparison experiment, we run another test particle simulation that is the same as the previous simulation, except that the Galactic bar is rotating with a constant pattern speed of $34\,\mathrm{km\,s^{-1}\,kpc^{-1}}$. The resulting age–metallicity plane is shown in panel (b) of Figure 1. A clear difference is that only one sequence is observed as the corotation resonance cannot drag particles from the inner Galaxy to the outer disk, but instead only mixes stars around the corotation radius. Other nonaxisymmetric perturbations (e.g., spiral arms) have to be involved in explaining the observation, which may lead to other inconsistencies (e.g., see C. Hamilton et al. 2024).

In panel (c) of Figure 1, we show the column-normalized age–metallicity distribution for the subgiant-star sample described in Section 2. As for the test particle simulation, there are two distinct sequences marked by the blue and orange dashed lines. The test particle simulation results suggest that the lower sequence is composed of stars that formed at $R \sim R_{\odot}$, and the upper sequence is composed of stars formed in the inner Galaxy that have migrated with the expansion of the corotation radius. M. Xiang & H.-W. Rix (2022) also pointed out the migration origin of the upper sequence. Under this scenario, the turning point in the upper sequence, indicated by
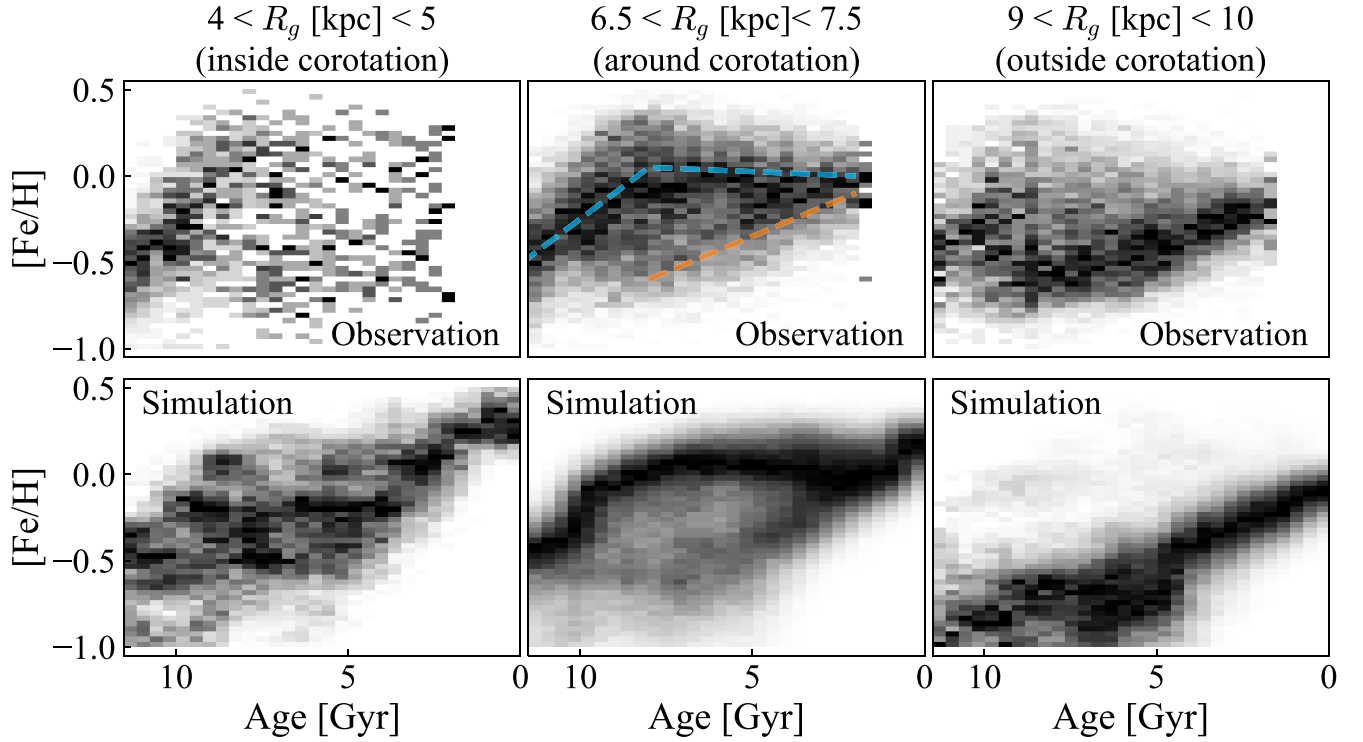
**Figure 2.** Top panels: the observed age–metallicity (column-normalized) distribution of the subgiant stars in various guiding radius bins. The blue and orange dashed lines in the middle panel denote the migrated and local age–metallicity sequence, which we will use in Figure 3. Bottom panels: the age–metallicity (column-normalized) distribution of the test particle simulation with a slowing-down bar in different guiding radius bins.

the red dashed–dotted line, gives an estimate of the bar formation epoch of ∼8 Gyr ago, which is broadly consistent with other measurements of the bar formation time (M. Haywood et al. 2024; J. L. Sanders et al. 2024). We indicate the metallicity and age of the Sun with the red circle in panel (c). The Sun resides on the migrated sequence, suggesting that the Sun may have migrated to its current location with the corotation of the bar (J. Baba et al. 2024). A difference between panels (a) and (c) is that the upper envelope of the migrated sequence in the observations is decreasing while its counterpart in the test particle simulation is flat. This implies that either the deceleration rate is underestimated (see discussion in Section 4.3.1) or other nonaxisymmetric perturbations neglected in the simulation have enhanced the radial migration.

*4.1.1. Age–Metallicity Sequences at Different Guiding Radii*

We further examine the dependence of the sequences in the age–metallicity plane on the guiding radii, $R_g$, of the stars. The upper (lower) panels of Figure 2 show the column-normalized age–metallicity distribution of stars (test particles) in guiding radius bins of $4 < R_g/\mathrm{kpc} < 5$, $6.5 < R_g/\mathrm{kpc} < 7.5$, and $9 < R_g/\mathrm{kpc} < 10$, corresponding to stars (test particles) that are inside, around, and outside the current corotation resonance, respectively (see the full plot of the age–metallicity distribution in all guiding radius bins in Figures B1 and B2). The distribution in the age–metallicity space strongly depends on the guiding radius in both the observation and simulation:

1. Inside the current corotation radius ($4 < R_g/\mathrm{kpc} < 5$, left column), we do not find a strong correlation in the age–metallicity plane, except for a sequence of increasing metallicity for stars older than ∼8 Gyr. This is the age–

metallicity relation sequence for the high-$\alpha$ disk discussed in M. Xiang & H.-W. Rix (2022; see Figure 2 therein). Fewer stars are observed at lower ages because of the imposed birth radius selection, which requires stars to have rather eccentric orbits to be born in the inner Galaxy and observed in the solar vicinity. As a result, the trends in the young stars are inconclusive. Similar shapes of the age–metallicity sequences have also been observed with the APOGEE data (J. Lian et al. 2022a; S. Khoperskov et al. 2024). The test particle simulation suggests that this guiding radius bin is dominated by stars born at this radius, but stars born inside and outside have nonnegligible contributions as well.

2. For the observed stars with a guiding radius around the present-day corotation radius ($6.5 < R_g/\mathrm{kpc} < 7.5$, middle column), the upper age–metallicity sequence dominates, but the lower sequence also appears, albeit only weakly. In the lower middle panel, the age–metallicity plane of the test particles also shows the coexistence of these two sequences.

3. Outside the corotation radius ($9 < R_g/\mathrm{kpc} < 10$, right column), the lower sequence in both the observation and the simulation dominates the age–metallicity plane. A similar result is also presented in J. Lian et al. (2022a) using the APOGEE survey.

The dependence of the age–metallicity distribution on the guiding radius sheds light on the origin of the two age–metallicity sequences. The observation that the upper sequence is strongest around the corotation radius further supports our argument that the stars in the upper sequence are migrated due to the corotation resonance. The guiding radii of stars trapped in corotation orbits oscillate around the corotation radii. The half peak-to-peak amplitude of this guiding radius oscillation in
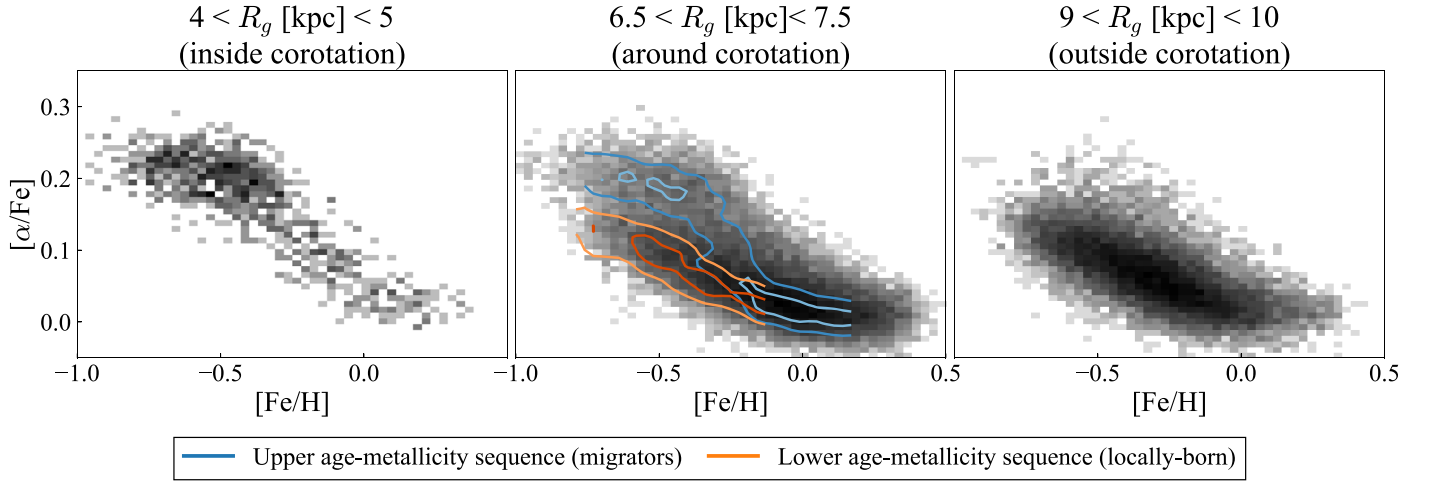
**Figure 3.** The (non-column-normalized) [$\alpha$/Fe]–[Fe/H] distribution of the observed stars in three guiding radius bins. In the middle panel, the blue (orange) contours show the column-normalized distribution of stars in the upper (lower) age–metallicity sequence, which we selected in the top middle panel in Figure 2.

the potential model we use is $\sim$1−1.6 kpc. Given that the present-day corotation radius is $\sim$6.5−7.5 kpc (R. Chiba & R. Schönrich 2021; D. Kawata et al. 2021; J. P. Clarke & O. Gerhard 2022; A. M. Dillamore et al. 2023, 2024a; C. Cao et al. 2024; H. Zhang et al. 2024b), we expect to see that the upper sequence exists only in guiding radius bins between 5 and 9 kpc, which is consistent with the observations (see Appendix B for more plots).

### 4.2. Implication for the Disk [α/Fe]-bimodality

Radial migration driven by a decelerating bar also naturally explains the [$\alpha$/Fe]-bimodality observed in the Galactic disk. We argue that the solar vicinity is occupied by stars with two different origins: stars formed in the inner Galaxy that have experienced resonant dragging, and stars formed around the solar circle. Due to the difference in birth environment for these two groups of stars, the distribution of the $\alpha$-element abundance, [$\alpha$/Fe], at the same metallicity should be different. Under the inside-out disk formation scenario and the [$\alpha$/Fe]–age relation of the Milky Way (A. Miglio et al. 2021), stars from the inner part of the Galactic disk are expected to be more $\alpha$-rich compared to outer disk stars at the same metallicity.

An [$\alpha$/Fe]-bimodality is reported in the LAMOST survey (M. Xiang et al. 2019; C. Wang et al. 2022). In Figure 3, we show the distribution of [$\alpha$/Fe]–[Fe/H] for stars in the same guiding radii chosen in Figure 2. We do not see an [$\alpha$/Fe]-bimodality inside or outside the current corotation radius, as shown in the left and right panels. We have already discussed how the guiding radius bin of 4–5 kpc is impacted by the selection function, which favors stars from the high-$\alpha$ thick disk. However, a similar result is also reported using the APOGEE survey, which should be less affected by this effect (M. R. Hayden et al. 2015; S. Sharma et al. 2021a). In the middle panel, which shows the [$\alpha$/Fe]–[Fe/H] distribution of stars around the corotation radius, the blue (orange) contour illustrates the column-normalized distribution of stars located around the upper (lower) age–metallicity sequence denoted by the blue (orange) dashed line in the upper middle panel of Figure 2. The [$\alpha$/Fe]–[Fe/H] distribution naturally separates into two distinct sequences, the sequence of migrated stars (high-[$\alpha$/Fe]), and the sequence of local stars (low-[$\alpha$/Fe]). The high-[$\alpha$/Fe] migrated stars are born in the inner Galaxy

($R \lesssim$ 4 kpc; see the next section) before the bar starts to decelerate. With the slowing of the Galactic bar, the corotation resonance picks up stars at larger Galactocentric radii, which have lower [$\alpha$/Fe] values, causing a quick drop in [$\alpha$/Fe] for the migrated sequence at higher metallicity. The orange sequence is composed of stars formed around the solar circle and hence has a lower [$\alpha$/Fe] value.

Our results supplement previous analyses that have shown that radial migration can reproduce the [$\alpha$/Fe]-bimodality in the Galactic disk (S. Sharma et al. 2021a; B. Chen et al. 2023). The scale length growth of the disk has to be more finely tuned to match the observed radial dependence of the [$\alpha$/Fe]–[Fe/H] plane for radial migration mechanisms that do not favor the current corotation radius. Our analysis suggests decelerating-bar-driven radial migration is the key mechanism responsible for the disk [$\alpha$/Fe]-bimodality, which causes the migrated and local stars to coexist around the present corotation radius, naturally. However, other effects in addition to radial migration could also cause [$\alpha$/Fe]-bimodality in the Galactic disk, and our results cannot rule out their existence (e.g., O. Agertz et al. 2021; S. Khoperskov et al. 2021; F. Renaud et al. 2021).

### 4.3. Inferred Slowdown History of the Galactic Bar

We have developed a qualitative picture of bar-driven radial migration and now turn to a more quantitative estimate of the required bar properties to explain the migrated age–metallicity sequence dragged by the bar corotation resonance. We describe a motivational model that gives an initial estimate and builds intuition for the effect before giving a fuller calculation utilizing a more realistic birth radius method.

#### 4.3.1. A Motivational Calculation

In a realistic galaxy model, the metallicities of stars depend on their birth time and radius, i.e., [Fe/H]($t, R$). Hence, the age–metallicity gradient of a sequence can be written as

$$\frac{D[\text{Fe/H}]}{Dt} = \frac{\partial[\text{Fe/H}]}{\partial R}\frac{dR}{dt} + \frac{\partial[\text{Fe/H}]}{\partial t}. \qquad (2)$$

Under the scenario that the migrated (upper) age–metallicity sequence is a consequence of the dragging of the bar corotation resonance, we relate $dR/dt$ to the bar deceleration rate as

follows:

$$\frac{dR_{CR}}{dt} = -\frac{\dot{\Omega}}{\Omega^2} V_c = \eta V_c. \quad (3)$$

We then rearrange Equation (2) as

$$\eta = \frac{\partial[Fe/H]/\partial t - D[Fe/H]/Dt}{|\partial[Fe/H]/\partial R|} \frac{1}{V_c}. \quad (4)$$

We can estimate $\partial[Fe/H]/\partial t$ from the slope of the local (lower) age–metallicity sequence in Figure 1, which yields $\partial[Fe/H]/\partial t \approx 0.075\,\mathrm{dex\,Gyr^{-1}}$. We adopt $V_c \approx 230\,\mathrm{km\,s^{-1}}$ and $\partial[Fe/H]/\partial R \approx -0.07\,\mathrm{dex\,kpc^{-1}}$ (P. J. McMillan 2017; G. A. Bragança et al. 2019). As the age–metallicity gradient of the migrated sequence is almost flat, $D[Fe/H]/Dt \approx 0$, we calculate $\eta \approx 0.0046$ from Equation (4). From Equation (2), we can see that the flatness of the migrated age–metallicity sequence is a consequence of the balance between the bar deceleration rate and the metallicity enrichment rate. A decline or increase in the migrated age–metallicity sequence after bar formation could also be expected if the deceleration rate is faster or slower.

### 4.3.2. Inference with the Birth Radii of Stars

We can decipher radial migration in the Galactic disk in greater detail with the inferred birth radii of stars. With stellar metallicity and age measurements, Y. L. Lu et al. (2024) improved on the method described in I. Minchev et al. (2018) and derived the empirical metallicity temporal evolution, $[Fe/H](R_b, \tau)$, with the same subgiant-star sample that we use in this work (M. Xiang & H.-W. Rix 2022). Using the metallicity evolution, they calculated the birth radii of these stars. The methodology is tested against various suites of cosmological simulations (see Y. L. Lu et al. 2022, 2024; Y. Lu et al. 2024; B. Ratcliffe et al. 2024b; and some details in Appendix C). In our analysis, we adopt the birth radii inferred in Y. L. Lu et al. (2024). By projecting the age–metallicity plane to the age–$R_b$ plane, we are able to study the radial migration history of the Galactic disk in detail.

Corotation orbits are characterized by their special orbital shape, in which the corotation stars spend the majority of their orbital lifetime along one side of the Galactic bar. To select stars that are in corotation resonance with the Galactic bar, we integrate the orbits from their present-day phase space location for $\sim$2 Gyr, and we classify a star as trapped in the corotation resonance if its orbit resides on one side of the Galactic bar over 95% of this time. The stars in the present-day corotation resonance are candidates for stars that have migrated with the decelerating bar. In the left panel of Figure 4, we show the column-normalized histogram of the age–$R_b$ plane for the test particle simulation in the background. The contours show the column-normalized distribution of the selected corotating stars. The blue line in the left panel indicates the temporal evolution of the corotation radius at different times in the test particle simulation, i.e., $R_{CR}(t)$ in Equation (1). The blue line coincides with the distribution of trapped stars, demonstrating that we can use the birth radii of the corotating stars to infer the temporal evolution of the corotation radii in the Milky Way.

We repeat the analysis using the observed data and the birth radii inferred in Y. L. Lu et al. (2024). To select corotating stars, we integrate the orbits assuming that the current bar angle and pattern speed are $25°$ and $34\,\mathrm{km\,s^{-1}\,kpc^{-1}}$ (H. Zhang et al. 2024b). In the right panel of Figure 4, we show the column-normalized distribution of all the stars in the background and that of the selected corotating stars by the contours. The contours for the corotating stars have very similar behavior to the test particle results, notably a plateau for the old stars and a linear increase for the young stars. We fit a function, $R_{CR}(\tau)$, to the innermost contour of the selected corotating stars using the least-squares method, where

$$R_{CR}(\tau) = \begin{cases} R_{CR,0}, & \tau > \tau_0, \\ R_{CR,0} + \eta V_c(\tau_0 - \tau), & \tau < \tau_0. \end{cases} \quad (5)$$

$R_{CR,0}$ is the initial corotation radius, $\tau_0$ the age that the Galactic bar starts to decelerate, $\eta = -\dot{\Omega}/\Omega^2$ the deceleration rate, and $V_c$ the rotation curve, of which we fix the value to $230\,\mathrm{km\,s^{-1}}$ (P. J. McMillan 2017). The best-fit line is shown in blue in the right panel of Figure 4. The best-fit values are $R_{CR,0} = 2.9\,\mathrm{kpc}$, $\eta = 0.0035$, and $\tau_0 = 7.2\,\mathrm{Gyr}$. The statistical uncertainties on
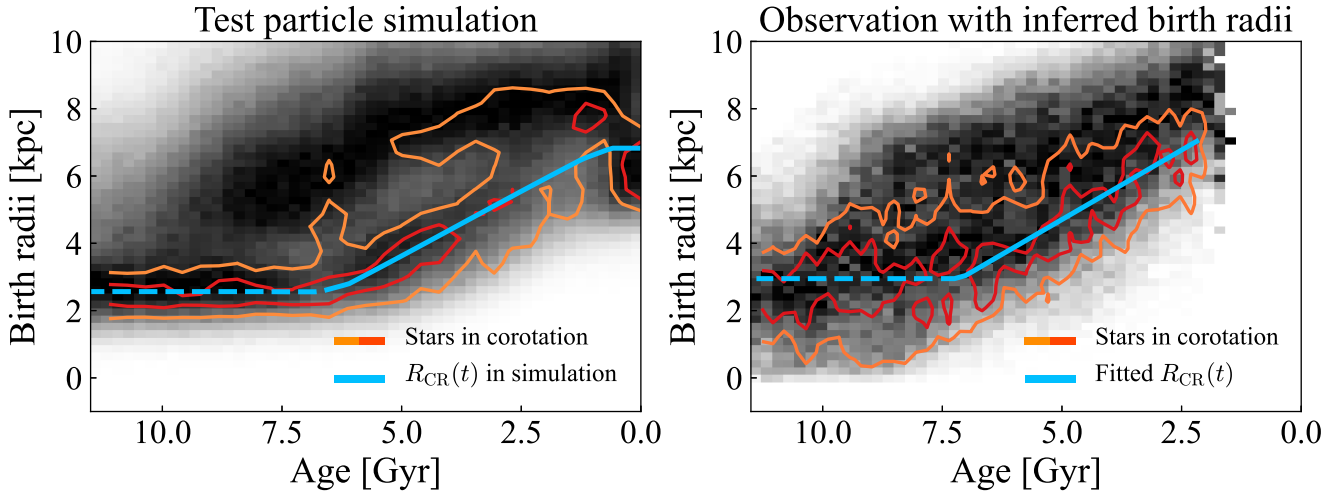


**Figure 4.** Left panel: the background is the column-normalized distribution of the test particles in the simulation in the age–birth radius ($R_b$) plane, and the contour shows the same distribution of the selected particles that are corotating with the bar. The blue line indicates the temporal evolution of the corotation radius in the test particle simulation, in which the dashed part is for the time before the bar formation, and the solid line is after the bar formation. Right panel: the same as the left panel but for the observed stars with the birth radii inferred in Y. L. Lu et al. (2024), and the contours are for the selected corotation stars. The blue line is fitted for the sequences of the corotation stars, from which we inferred the slowing-down history of the Galactic bar.
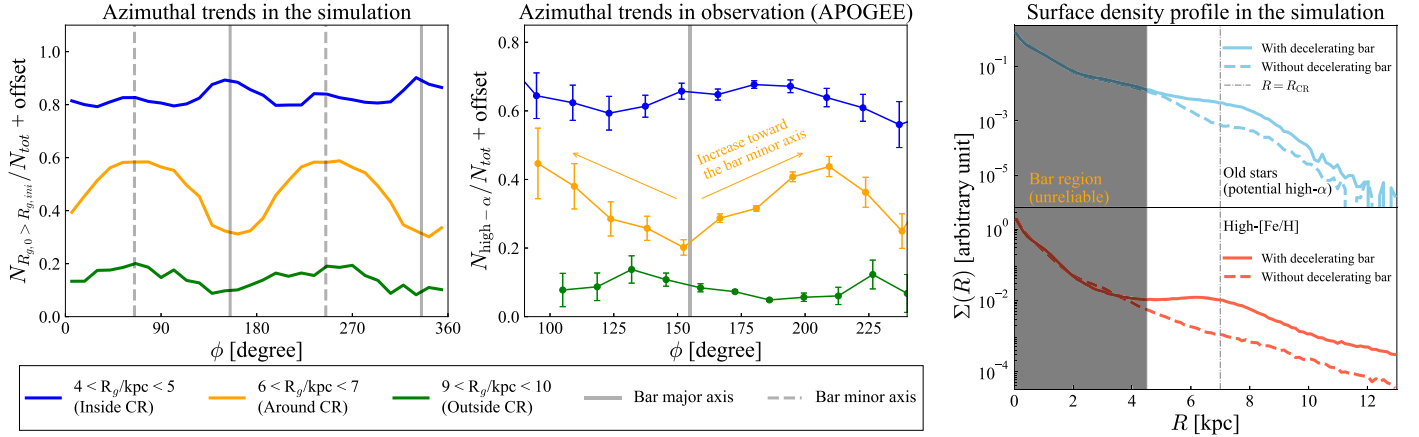
**Figure 5.** Left: the fraction of outward-migrated stars as a function of azimuthal angle in different guiding radius bins. The vertical solid and dashed lines denote the bar major and minor axes. Middle: the observed fraction of high-$\alpha$ stars as a function of azimuthal angle. Right: the radial surface density profile of old stars/high-[Fe/H] stars in the test particle simulation with a decelerating bar (solid lines) and with a constant pattern speed bar (dashed lines). The vertical dashed line represents the current corotation radius.

these parameters are significantly smaller than the systematic uncertainties discussed later. The inferred slowing-down rate is similar to the previous approximate calculation and is consistent with the measurement in R. Chiba et al. (2021). The best-fit $\tau_0$ is consistent with previous measurements of the bar formation time (M. Haywood et al. 2024; J. L. Sanders et al. 2024). With the best-fit $R_{CR,0} = 2.9$ kpc, the initial pattern speed is then $\Omega_0 \sim 80$ km s$^{-1}$ kpc$^{-1}$. These parameters agree with the pattern speed evolution of Milky Way–type galaxies in the TNG50 cosmological simulation suite (M. Semczuk et al. 2024).

Since the history of the Milky Way is mostly unknown, the birth radius inference in Y. L. Lu et al. (2024) requires a few assumptions to obtain the metallicity evolution. Here, we experiment with adjusting the calibrated metallicity evolution model in Y. L. Lu et al. (2024) to assess the systematic uncertainties in the deceleration rate inference. By shifting the present-day metallicity at the Galactic center ($\pm 0.1$ dex) and the value of the steepest metallicity gradient ($\pm 15\%$), we rederive the birth radii of stars in our sample. We find that the general shape of the distribution of the corotating stars in the age–$R_b$ plane remains the same, but the exact values of the best-fit parameters vary. The parameters vary in the range of $\tau_0 \sim 6$–$8$ Gyr, $\eta \sim 0.0025$–$0.0040$, and $\Omega_0 \sim 60$–$100$ km s$^{-1}$ kpc$^{-1}$. The variation of the initial pattern speed is the highest as the value is sensitive to even a small variation in $R_b$. These variations show the order of magnitude of the systematic uncertainty in our inference. We also vary the bar angle ($\pm 5°$) and the present-day pattern speed ($\pm 5$ km s$^{-1}$ kpc$^{-1}$) needed to select the corotating stars, but these give variations in the best-fit parameters that are significantly smaller than the systematic uncertainties induced by the birth radius inference method.

## 5. Discussion

### 5.1. Predictions for the Bar-driven Radial Migration Scenario

In addition to the results shown above, there is more observational evidence to support decelerating-bar-driven radial migration as the main driver for the migration in the Milky Way disk.

*Azimuthal metallicity variation*. P. Di Matteo et al. (2013) showed that ongoing radial migration can cause azimuthal abundance variations in the galactic disk. A key difference in the bar-driven radial migration scenario from other migration mechanisms is the azimuthal distribution of the migrated stars. Due to the characteristic shape of the corotation orbits, corotating stars naturally clump along the bar minor axis around the corotation radius. Therefore, the stars that experienced corotation dragging and migrated from the inner Galaxy would form an overdensity along the bar minor axis as shown in the left panel of Figure 5, causing the mean metallicity to peak along the bar minor axis. To demonstrate this, we use our decelerating bar test particle simulation without the solar neighborhood cut to show the fraction of outward-migrated stars as a function of azimuthal angle in different guiding radius bins, as shown in the left panel of Figure 5. The orange line illustrates a clear azimuthal dependence in the spatial distribution of the migrated stars around the corotation resonance. Azimuthal metallicity variation has been observed in the Milky Way disk (E. Poggio et al. 2022; K. Hawkins 2023; Z. Hackshaw et al. 2024). Recently, S. Khoperskov et al. (2024) measured the metallicity distribution of the entire Galactic disk with orbital reconstruction. As shown in Figure 22 therein, the metallicity for stars around guiding radii of 7 $-8$ kpc varies sinusoidally in the azimuthal direction and peaks along the bar minor axes. Such an azimuthal trend is not seen in stars at other guiding radii. This result is in agreement with the prediction of our model. However, kinematic fragmentation (V. P. Debattista et al. 2017; F. Fragkoudi et al. 2017; H. Zhang et al. 2024c) could also cause a similar result, as kinematically cold (more metal-rich) stars are easier to trap. Therefore, more analysis is needed to differentiate these mechanisms.

*Azimuthal variation in the high-$\alpha$ star fraction*. As we discussed in Section 4.2, high-$\alpha$ stars observed in the solar vicinity are members of the migrated star sequence. Therefore, similar to the metallicity, we might also expect an azimuthal variation for the high-$\alpha$ star fraction ($N_{high-\alpha}/N_{total}$), where more high-$\alpha$ stars are expected along the bar minor axes. As shown in the middle panel of Figure 5, we examine this using a subsample of APOGEE DR17, following the quality cuts we address in detail in Appendix D. We indeed see an azimuthal variation in the fraction of high-$\alpha$ stars around the corotation

radius, while the variation is much smaller outside the corotation radius. The fraction is smallest around the bar's major axis and increases toward the minor axis. The prediction is also in agreement with the results shown in S. Khoperskov et al. (2024), who found that the high-$\alpha$ sequence contributes more in the direction of the minor axes than in that of the major axes.

*Coldness of the Galactic disk.* N. Frankel et al. (2020) found that diffusion in the angular momentum of the Galactic disk stars is much greater than the scattering of radial actions. Recently, C. Hamilton et al. (2024) showed that it is difficult to transport stars with such coldness with transient spiral arms unless the lifetime and pitch angle for the spiral arms are fine-tuned (but also see the counterevidence in J. A. Sellwood & J. Binney 2025). However, in the bar-driven radial migration scenario, the angular momentum of the corotating stars increases with the slowing of the bar, but the radial actions are invariant (see J. A. Sellwood & J. J. Binney 2002; R. Chiba et al. 2021 for theoretical explanations). Computationally, S. Khoperskov et al. (2020) showed that the orbits of stars transported with the corotation resonance can remain circular. So, the bar-driven radial migration scenario can alleviate the problem of the coldness of the migration, but more experiments or quantitative analysis is required to demonstrate which fraction of the slowing-bar-driven migration is needed to explain the observation.

*Density profile of the disk.* As argued, the Galactic high-$\alpha$ and high-Fe disk should also experience significant radial migration driven by the decelerating bar. Stars that experienced resonant dragging clump around the present-day corotation radius producing a maximum in the radial exponential surface density profile of the high-$\alpha$ and high-Fe (supersolar) disk leading to the broken power law profiles observed by previous studies (Z. Yu et al. 2021; J. Lian et al. 2022b). We demonstrate the role of the decelerating bar using our simulations in the right panel of Figure 5. We show the surface density profile of the simulation with a decelerating bar (in solid lines) and with a constant pattern speed bar (in dashed lines) for an old population (age $> 8$ Gyr, potentially high-$\alpha$ stars in the Milky Way) and a high-[Fe/H] population ([Fe/H] $> 0.2$). The surface density profiles of both populations deviate from the initial exponential profile around the current corotation resonance in the presence of a decelerating bar. As other mechanisms may also lead to a broken power law density profile, more studies are required to build the unique correlation between the disk's density profiles and the bar-driven radial migration mechanism.

### 5.2. Caveats of the Test Particle Simulation

Our test particle simulations have a number of simplifications and limitations.

First, we kept the bar strength constant since the bar's formation. However, a realistic bar may experience a buckling instability during its evolution. When bar buckling occurs, the bar strength drops rapidly and many stars trapped by the corotation resonance may escape (S. Khoperskov et al. 2020). Hence, the efficiency of radial migration could have been overestimated in the test particle simulation. Nevertheless, the resonant drag of the Galactic bar should still migrate the stars after the bar buckling, so it would not affect our argument. Similarly, the test particle simulation and our quantitative model in Section 4.3.2 both assumed a constant slowdown, $\eta$,

of the bar over its lifetime. Cosmological simulations (e.g., TNG50 as analyzed by M. Semczuk et al. 2024) show a diversity of slowdown histories (and even of periods of spin-up) so it is likely the Milky Way's bar history is more complex than our simple model. This simplifying assumption could then lead to an overestimation of the resonant trapping efficiency and hence of the migration efficiency.

Second, the initial conditions of stellar particles released to the test particles after bar formation are in disequilibrium with the potential in the bar region because the initial conditions are axisymmetric while the potential is barred. This leads to an unrealistic simulation result in the bar region, but stellar particles born outside the bar region are less affected by this issue as the nonaxisymmetric component of the potential becomes weaker. As we mainly analyze the corotation resonance and stars around it, which is constantly outside the bar region in the simulation setup, this issue would not impact our conclusion much.

Third, we adopted a specific chemical model to assign the metallicity of the particles in the simulation. The detailed quantitative results presented in this work depend on the method in Y. L. Lu et al. (2024). However, the nature of our argument is that the decelerating-bar-driven radial migration causes stars from very different birth radii to coexist around the corotation radius, and the metallicity of the migrated sequence naturally flattens after the bar formation because the corotation resonance moves outward. Hence, switching to a different chemical model does not affect our argument as long as the radial metallicity gradient in the model is reasonable. Furthermore, our motivational calculation in Section 4.3.1 and the observation of a break in the upper migrated age–metallicity sequence are direct empirical indicators that lead to very similar conclusions to the more detailed birth radius calculation.

### 6. Conclusion

In this work, we analyzed the age–metallicity distribution of subgiant stars in the solar vicinity and observed two distinct age–metallicity sequences (see panel (c) of Figure 1 for the observed age–metallicity plane). We ran a test particle simulation with a decelerating bar. The corotation resonance of the Galactic bar sweeps through the disk trapping particles. These trapped particles then experience resonant dragging and migrate with the expansion of the corotation radius. The simulation reproduces the two distinct sequences in age–metallicity: the upper age–metallicity sequence corresponds to stars formed in the inner Galaxy that have migrated with the corotation resonance, while the lower sequence is composed of stars formed locally around the solar circle that have not undergone much radial migration. This explains the rapid metallicity increase at early times, the flattening at late times in the migrated sequence, and the strong age–metallicity correlation in the local sequence.

We further showed the guiding radius dependence of the upper and lower age–metallicity sequences. The upper sequence is the dominant population around the present-day corotation radius, whereas the lower sequence dominates outside the corotation radius. We observed the upper sequence in the guiding radius bins of $\sim 5.5-9$ kpc, which is consistent with the expected radial range of the current corotation resonance and the amplitude of the libration oscillation (R. Chiba & R. Schönrich 2021; R. Chiba et al. 2021). We

found the same guiding radius dependence in our test particle simulation, strengthening the conclusion that this sequence is composed of migrators dragged by the corotation resonance.

We provided a series of other predictions if the slowing down of the Galactic bar is the main driver responsible for the radial migration in the Milky Way disk. We expect that (1) the mean metallicity of stars is higher along the bar's minor axis around the corotation radius; (2) the fraction of high-$\alpha$ stars is smallest along the bar's major axis and increases toward the minor axis around the corotation radius, which is demonstrated in Figure 5 using the APOGEE survey; (3) the migrated stars experienced much more radial migration than radial heating; and (4) the radial density profile of the high-$\alpha$ and high-Fe stars should be consistent with a broken power law with a break close to the corotation radius. As discussed in Section 5.1, many of these predictions are consistent with observations in the Milky Way.

We also shed light on the origin of the disk [$\alpha$/Fe]-bimodality. Previous studies have discovered that radial migration could cause [$\alpha$/Fe]-bimodality of the disk (R. Schönrich & J. Binney 2009; I. Minchev et al. 2013; S. Sharma et al. 2021a; B. Chen et al. 2023). Here, we propose that migration driven by the decelerating bar could be the major mechanism, as the existence of the [$\alpha$/Fe]-bimodality also shows a clear dependence on the guiding radii and it is perhaps most prominent around the present-day corotation resonance of the bar. We show that the two distinct age–metallicity sequences occupy different regions in the [$\alpha$/Fe]–[Fe/H] plane, resulting in the [$\alpha$/Fe]-bimodality (S. Khoperskov et al. 2024).

Finally, under the radial migration scenario, we used the ages and metallicities of stars currently trapped at corotation to infer the evolution history of the Galactic bar's pattern speed. We used the birth radii inferred in Y. L. Lu et al. (2024) to track the temporal evolution of the corotation radius in the Milky Way's past. The results suggest that the Galactic bar formed and started to decelerate at $\tau_0 \sim 6-8$ Gyr with an initial pattern speed of $\Omega_0 \sim 60-100$ km s$^{-1}$ kpc$^{-1}$ and a constant slowdown rate $\eta \sim 0.0025-0.0040$, consistent with previous constraints (R. Chiba & R. Schönrich 2021; R. Chiba et al. 2021; M. Haywood et al. 2024; J. L. Sanders et al. 2024).

## Appendix A
## Details of the Test Particle Simulation

In this appendix, we describe the details of the test particle simulation we use in this work.

### A.1. Time Evolution of the Galactic Potential

We follow the same approach as in A. M. Dillamore et al. (2024a), except that we use a different bar formation time. We adopt the Milky Way potential in M. C. Sormani et al. (2022), which is an analytic approximation for the made-to-measure model of the inner Galaxy (M. Portail et al. 2017). We use the nonaxisymmetric part of this potential as a model of the Galactic bar. We run the test particle simulation for $\sim 11.5$ Gyr. The axisymmetric component of the potential is kept the same throughout the simulation so that the total mass is conserved. We let the bar component grow at $t_0 \sim 4$ Gyr from the start of the simulation and reach its maximum strength at $t_1 \sim 5$ Gyr, during which the pattern speed of the growing bar is constant. The smooth growth of the bar strength follows the same prescription in W. Dehnen (2000).

We set the initial pattern speed of the Galactic bar to $\Omega_i = 80$ km s$^{-1}$ kpc$^{-1}$. The Galactic bar starts to decelerate after it reaches its full strength. We slow the Galactic bar using a constant slowdown rate $\eta = 0.003$ ($\eta = -\dot{\Omega}/\Omega^2$), which is roughly consistent with the value obtained for the Milky Way bar in R. Chiba et al. (2021). The exact formula for the Galactic bar pattern speed evolution is as follows (R. Chiba et al. 2021; A. M. Dillamore et al. 2024a):

$$\Omega(t) = \begin{cases} \Omega_i & ,t_0 < t < t_1 \\ \Omega_i\left[1 + \frac{1}{2}\eta\Omega_i(t-t_1)^2/(t_2-t_1)\right]^{-1} & ,t_1 < t < t_2 \\ \Omega_2[1 + \eta\Omega_2(t-t_2)]^{-1} & ,t_2 < t < t_3 \\ \Omega_4\left[1 + \frac{1}{2}\eta\Omega_4(t-t_4)^2/(t_3-t_4)\right]^{-1} & ,t_3 < t < t_4 \\ \Omega_4 & ,t > t_4 \end{cases}$$

$$\Omega_2 = \Omega_i\left[1 + \frac{1}{2}\eta\Omega_i(t_2-t_1)\right]^{-1}$$
$$t_3 = \frac{2}{\eta\Omega_4} - \frac{2}{\eta\Omega_2} + 2t_2 - t_4,$$

where the initial pattern speed is $\Omega_i = 80$ km s$^{-1}$ kpc$^{-1}$, the final pattern speed is $\Omega_4 = 34$ km s$^{-1}$ kpc$^{-1}$, $t_0 \sim 4$ Gyr, $t_1 \sim 5$ Gyr, $t_2 \sim 5.5$ Gyr, and $t_4 \sim 11.2$ Gyr. We also adjust the length of the bar scaled to its corotation radius so that the length of the bar matches its original value when the pattern speed is $39$ km s$^{-1}$ kpc$^{-1}$ (the pattern speed value of the M. Portail et al. 2017 model). At the end of the simulation, the pattern speed is $34$ km s$^{-1}$ kpc$^{-1}$.

### A.2. Initial Condition of the Test Particles

The initial conditions of the stellar particles are generated from a quasi-isothermal disk model $f(\boldsymbol{J})$ (J. Binney 2010):

$$f(\boldsymbol{J}) \;=\; \frac{\tilde{\Sigma}\,\Omega_c}{2\pi^2\,\kappa^2} \times \frac{\kappa}{\tilde{\sigma}_r^2}\exp\!\left(-\frac{\kappa\,J_r}{\tilde{\sigma}_r^2}\right)$$
$$\times\; \frac{\nu}{\tilde{\sigma}_z^2}\exp\!\left(-\frac{\nu\,J_z}{\tilde{\sigma}_z^2}\right) \times B(J_\phi),$$

$$B(J_\phi) \;=\; \begin{cases} 1 & \text{if } J_\phi \geqslant 0, \\[2mm] \exp\!\left(\dfrac{2\Omega_c\,J_\phi}{\tilde{\sigma}_r^2}\right) & \text{if } J_\phi < 0, \end{cases}$$

$$\tilde{\Sigma}(R_c) \;\equiv\; \Sigma_0\exp(-R_c/R_{\text{disk}}),$$
$$\tilde{\sigma}_r^2(R_c) \;\equiv\; \sigma_{r,0}^2\exp(-2(R_c - R_0)/R_{\sigma,r}),$$
$$\tilde{\sigma}_z^2(R_c) \;\equiv\; \sigma_{z,0}^2\exp(-2(R_c - R_0)/R_{\sigma,z}),$$

where $J_r$, $J_\phi$, and $J_z$ are the radial, azimuthal, and vertical actions; $\kappa$ and $\nu$ are the radial and vertical epicyclic frequencies; and $\Omega_c$ is the circular angular frequency. The adopted parameters are $R_0 = 8$ kpc, $R_{\sigma,r} = R_{\sigma,z} = 5$ kpc, and $\sigma_{r,0} = \sigma_{z,0} = 10$ km s$^{-1}$. We increase the scale length, $R_{\text{disk}}$, of the disk model linearly from 1 kpc at the beginning of the simulation to 3.5 kpc at the end to mimic inside-out disk formation. We generate stars using the sampling routine in AGAMA (E. Vasiliev 2019). We release 10,000 particles into the test particle simulation every $\sim$100 Myr.

### A.3. Dynamical Heating

In addition to the heating induced by the growing bar, we give a random velocity kick to the particles in the simulation by convolving their three Cartesian velocities with an isotropic Gaussian distribution $\mathcal{N}(1, 0.03)$ every $\sim$100 Myr. This simulates the additional contribution of other scattering processes, e.g., those associated with spirals, satellites etc. The resulting radial velocity dispersion for stars at $R = 8$ kpc with age of 10 Gyr in the test particle simulation is $\sim$60 km s$^{-1}$, which is compatible with the observation in the Milky Way (S. Sharma et al. 2021b).

### A.4. Metallicity Assignment

With the birth radius and age of a star, we assign metallicities to the particles in the simulation using the metallicity enrichment derived in Y. L. Lu et al. (2024), [Fe/H]$(R_b, \tau)$, where $R_b$ is the birth radius of the particle. The method is calibrated for the LAMOST subgiant sample in M. Xiang & H.-W. Rix (2022). The method assumes a monotonic increase in stellar metallicity at the Galactic center and the radial metallicity gradient is constant throughout the time since the disk formation. In their method, the current metallicity gradient is $-0.07$ dex kpc$^{-1}$, taken from G. A. Bragança et al. (2019), and the highest metallicity is 0.6 dex in the Galactic center. The steepest metallicity gradient is $-0.15$ dex kpc$^{-1}$ at 8 Gyr ago, similar to what is seen in cosmological simulations. A more detailed description of the method is provided in Appendix C. Using this method,
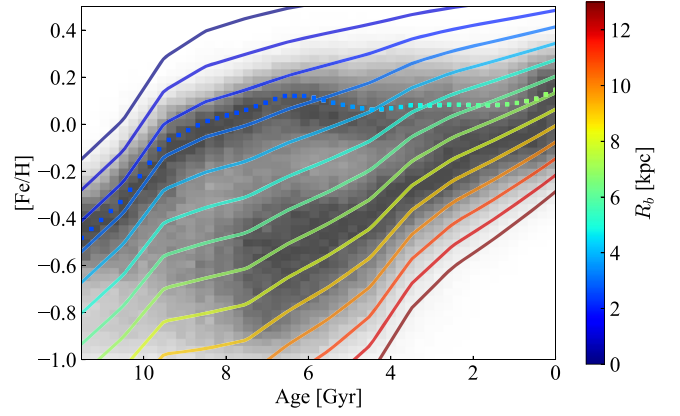


**Figure A1.** The model used for the metallicity assignment. Lines with different colors correspond to the metallicity evolution at different radii. The background shows the results of the test particle simulation with the decelerating bar. The dots denote the trend of [Fe/H](age, $R_{\text{CR}}$).

metallicity could also serve as an indicator for the birth radius of the particle, under which assumption more metal-rich stars are formed in the inner part of the Galaxy at the same ages. The detailed metallicity growth at different radii is presented in Figure A1.

We directly use this observationally calibrated method for the metallicity assignment in our test particle simulation for a better comparison between the observation and simulation, as we run the simulation from approximately the same age as the Milky Way disk formation. In Figure A1, we demonstrate that the (upper) migrated age–metallicity sequence follows the metal enrichment at the initial corotation radius before the bar formation and then crosses the age–metallicity relation at larger birth radii at a late time, causing its flattening.

## Appendix B
## Age–Metallicity Distribution in All Guiding Radius Bins

We present the age–metallicity distribution of stars and test particles in guiding radius bins of 4–5 kpc, 6.5–7.5 kpc, and 9–10 kpc. Here, we show a more complete picture of the age–metallicity distribution with all guiding radius bins from 4 to 13 kpc with a width of 0.5 kpc. Figure B1 shows the distribution for the observations and Figure B2 that for the test particle simulation. The orange dashed line in each panel of Figure B1 is used to separate the upper and lower sequences, and the orange dashed line in Figure B2 is used to denote the expected occupation for the distribution of particles transported by the corotation resonance (the same as the blue dashed line in Figure 1).

The final corotation radius in the test particle simulation is $\sim$7 kpc similar to the expected value for the Milky Way ($\sim$6.5$-$7.5 kpc). The amplitude of the guiding radius libration oscillation is $\sim$1$-$1.6 kpc, and hence, the corotation stars are expected to occupy the guiding radius range of $\sim$5–9 kpc. In both the observation and the test particle simulation, the upper sequence exists ubiquitously among this range of guiding radii and thus agrees with the expectation from the bar-driven radial migration scenario.
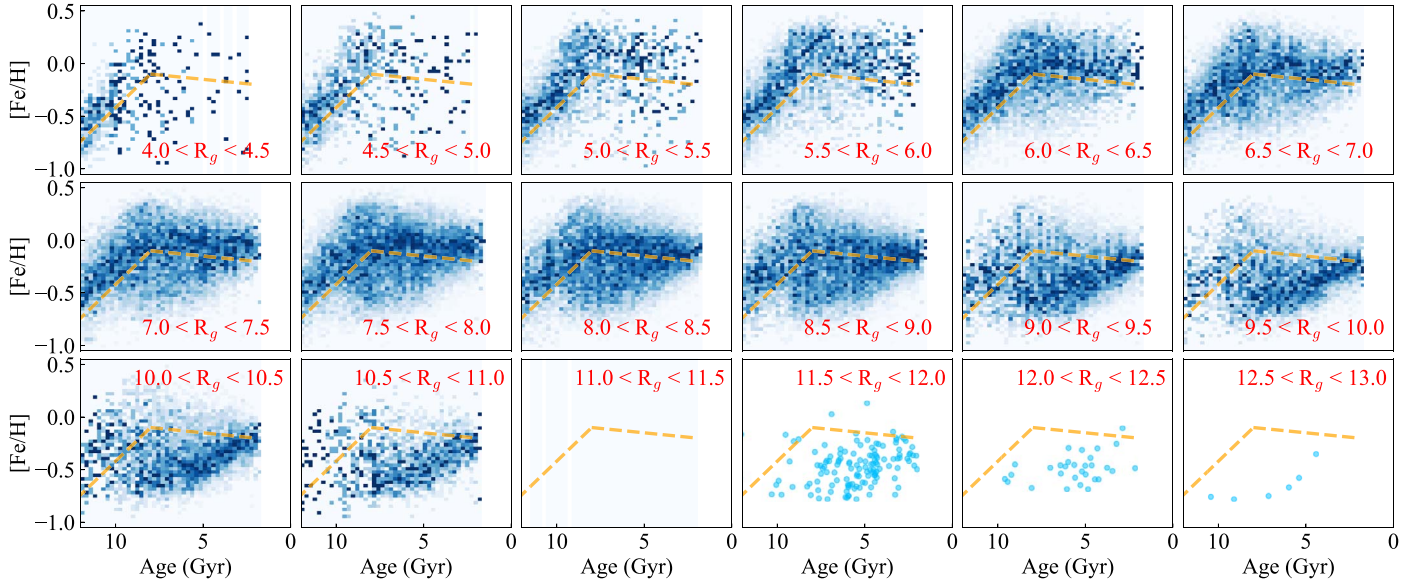
**Figure B1.** The age–metallicity distribution of the observed subgiant stars (M. Xiang & H.-W. Rix 2022) in different guiding radius bins, each with width of 0.5 kpc. The orange dashed lines denote the separation between the upper and lower sequences.
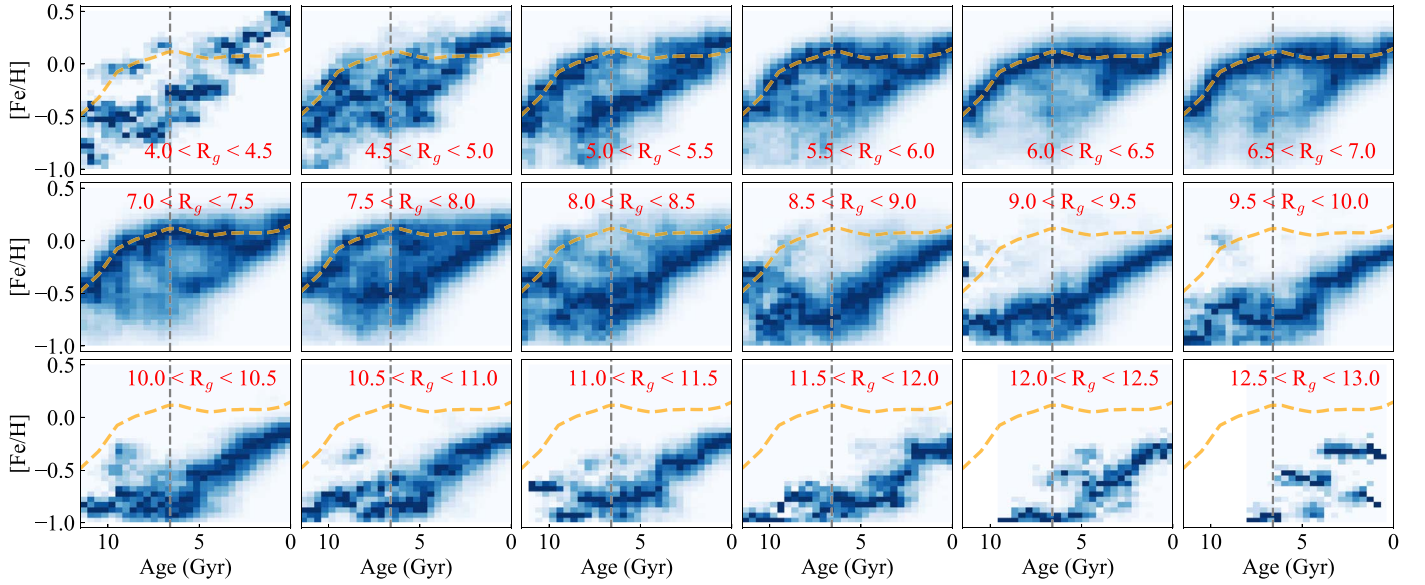


**Figure B2.** The age–metallicity distribution of the test particles (with a slowing-down bar) in different guiding radius bins. The orange dashed lines denote the sequence of particles that migrated with the expansion of the corotation radius. We draw attention to the similarity between the observation and simulation around and outside the corotation.

## Appendix C
## Birth Radius Calculation

The birth radii of stars are key information for decoding the radial migration in the Galactic disk. Y. L. Lu et al. (2024) improved on the method described in I. Minchev et al. (2018) to derive the birth radii of subgiant stars in M. Xiang & H.-W. Rix (2022). The method assumes that the radial metallicity gradient in the interstellar medium is always linear after the stellar disk started to form (tested using cosmological simulations in Y. L. Lu et al. 2022), following which we then can write the stellar metallicity for a star with age, $\tau$, and birth radius $R_b$ as

$$[\text{Fe/H}](R_b, \tau) = [\text{Fe/H}](R_b = 0, \tau) + \nabla [\text{Fe/H}](\tau) \times R_b, \quad \text{(C1)}$$

where $[\text{Fe/H}](R_b = 0, \tau)$ represents the central metallicity, and $\nabla[\text{Fe/H}](\tau)$ the metallicity gradient at the age. The central metallicity is estimated using the upper envelope of the observed age–metallicity plane at the corresponding age. Y. L. Lu et al. (2024) postulated that the metallicity gradient at a specific age is linearly correlated with the stellar metallicity range observed at that age, $\Delta[\text{Fe/H}](\tau)$, based on the simulated galaxies in NIHAO-UHD (T. Buck et al. 2020) and HESTIA (N. I. Libeskind et al. 2020). The linear correlation is written in the normalized metallicity range, $\Delta\widehat{[\text{Fe/H}]}$, which lies between 0 and 1, and

$$\nabla[\text{Fe/H}](\tau) = a\Delta\widehat{[\text{Fe/H}]} + b. \quad \text{(C2)}$$

Recently, B. Ratcliffe et al. ([2024a](#)) further corrected this correlation by adding the impact of the size of the star-forming region for the galaxy. The parameters in this linear correlation are determined using the boundary condition that the current metallicity gradient in the Galactic disk is $-0.07\,\mathrm{dex\,kpc}^{-1}$ (G. A. Bragança et al. [2019](#)), and the steepest metallicity gradient in the past. The latter is constrained by requiring that the youngest stars have close-to-zero migration and the disk forms inside out on a reasonable timescale, which leads to a value of $-0.15\,\mathrm{dex\,kpc}^{-1}$, similar to what is found in cosmological simulations. With $[\mathrm{Fe/H}](R_b, \tau)$, we can then rewrite Equation ([C1](#)) as

$$R_b = \frac{[\mathrm{Fe/H}]_{\mathrm{observed}} - [\mathrm{Fe/H}](R_b = 0, \tau)}{\nabla[\mathrm{Fe/H}](\tau)}. \tag{C3}$$

The assumptions and methodology are tested and verified against the NIHAO-UHD (T. Buck et al. [2020](#)) simulations in Y. L. Lu et al. ([2022](#)). They have also been tested on HESTIA (N. I. Libeskind et al. [2020](#); S. Khoperskov et al. [2023](#)) and TNG50 (D. Nelson et al. [2019](#)) for Milky Way–like galaxies (B. Ratcliffe et al. [2024b](#)) and NIHAO galaxies (L. Wang et al. [2015](#)) down to the LMC mass (Y. Lu et al. [2024](#)).

## Appendix D
## Azimuthal Variation for High-$\alpha$ Star Fraction

We use the metallicity and $[\alpha/\mathrm{M}]$ measured in the APOGEE survey (Abdurro'uf et al. [2022](#)) as it has a larger azimuth coverage than the LAMOST subgiant sample we use for the main results. As in the data selection in Section [2](#), we keep stars with small distance uncertainty, small metallicity uncertainty, and small $[\alpha/\mathrm{M}]$ uncertainty, i.e., $\varpi/\sigma_\varpi > 5$, $\sigma_{[\mathrm{M/H}]} < 0.02$, and $[\alpha/\mathrm{M}] < 0.05$. Stars with $[\mathrm{M/H}] > -1$ are removed for disk star selection. We only analyze stars with $0.5 < |z|/\mathrm{kpc} < 1.5$ to ensure that the $z$-distributions of the selected stars are roughly the same at each azimuthal angle.

We classify a star as a high-$\alpha$ star if $[\alpha/\mathrm{M}] > 0.18$ for $[\mathrm{M/H}] < -0.7$ or $[\alpha/\mathrm{M}] > 0.18 - 0.01([\mathrm{M/H}] + 0.7)$ for $[\mathrm{M/H}] \geqslant -0.7$. We then take the ratio of the high-$\alpha$ to the total stars at different azimuthal angles in each of the guiding radius bins as shown in the middle panel of Figure [5](#). There is an obvious increase of the high-$\alpha$ star fraction for the azimuthal angles away from the bar major axis around the present-day guiding radii ($6 < R_g/\mathrm{kpc} < 7$), while the variation is much more insignificant inside and outside the corotation. This is in agreement with the expected consequence of radial migration driven by the decelerating bar (see more discussion in Section [5.1](#)).

## ORCID iDs

HanYuan Zhang ● https://orcid.org/0009-0005-6898-0927
Vasily Belokurov ● https://orcid.org/0000-0002-0038-9584
N. Wyn Evans ● https://orcid.org/0000-0002-5981-7360
Jason L. Sanders ● https://orcid.org/0000-0003-4593-6788
Yuxi(Lucy) Lu ● https://orcid.org/0000-0003-4769-3273
Chengye Cao ● https://orcid.org/0000-0001-6655-854X
GyuChul Myeong ● https://orcid.org/0000-0002-5629-8876
Adam M. Dillamore ● https://orcid.org/0000-0003-0807-5261
Sarah G. Kane ● https://orcid.org/0000-0001-8411-1012
Zhao-Yu Li ● https://orcid.org/0000-0001-5017-7021

## References

Abdurro'uf, Accetta, K., Aerts, C., et al. 2022, ApJS, 259, 35
Agertz, O., Renaud, F., Feltzing, S., et al. 2021, MNRAS, 503, 5826
Astropy Collaboration, Price-Whelan, A. M., Sipőcz, B. M., et al. 2018, AJ, 156, 123
Astropy Collaboration, Robitaille, T. P., Tollerud, E. J., et al. 2013, A&A, 558, A33
Athanassoula, E. 1992, MNRAS, 259, 345
Athanassoula, E. 2003, MNRAS, 341, 1179
Baba, J., Tsujimoto, T., & Saitoh, T. R. 2024, ApJL, 976, L29
Bailer-Jones, C. A. L., Rybizki, J., Fouesneau, M., Demleitner, M., & Andrae, R. 2021, AJ, 161, 147
Belokurov, V., & Kravtsov, A. 2022, MNRAS, 514, 689
Belokurov, V., & Kravtsov, A. 2024, MNRAS, 528, 3198
Beraldo e Silva, L., Debattista, V. P., Nidever, D., Amarante, J. A. S., & Garver, B. 2021, MNRAS, 502, 260
Binney, J. 2010, MNRAS, 401, 2318
Binney, J. 2020, MNRAS, 495, 895
Bland-Hawthorn, J., & Gerhard, O. 2016, ARA&A, 54, 529
Bovy, J., Leung, H. W., Hunt, J. A. S., et al. 2019, MNRAS, 490, 4740
Bragança, G. A., Daflon, S., Lanz, T., et al. 2019, A&A, 625, A120
Buck, T., Obreja, A., Macciò, A. V., et al. 2020, MNRAS, 491, 3461
Cao, C., Li, Z.-Y., Schönrich, R., & Antoja, T. 2024, ApJ, 975, 292
Carr, C., Johnston, K. V., Laporte, C. F. P., & Ness, M. K. 2022, MNRAS, 516, 5067
Chandra, V., Semenov, V. A., Rix, H.-W., et al. 2024, ApJ, 972, 112
Chen, B., Hayden, M. R., Sharma, S., et al. 2023, MNRAS, 523, 3791
Chiba, R., Friske, J. K. S., & Schönrich, R. 2021, MNRAS, 500, 4710
Chiba, R., & Schönrich, R. 2021, MNRAS, 505, 2412
Clarke, J. P., & Gerhard, O. 2022, MNRAS, 512, 2171
Conroy, C., Weinberg, D. H., Naidu, R. P., et al. 2022, arXiv:2204.02989
Daniel, K. J., Schaffner, D. A., McCluskey, F., Fiedler Kawaguchi, C., & Loebman, S. 2019, ApJ, 882, 111
Debattista, V. P., Ness, M., Gonzalez, O. A., et al. 2017, MNRAS, 469, 1587
Debattista, V. P., & Sellwood, J. A. 2000, ApJ, 543, 704
Dehnen, W. 2000, AJ, 119, 800
Deng, L.-C., Newberg, H. J., Liu, C., et al. 2012, RAA, 12, 735
Dillamore, A. M., Belokurov, V., & Evans, N. W. 2024a, MNRAS, 532, 4389
Dillamore, A. M., Belokurov, V., Evans, N. W., & Davies, E. Y. 2023, MNRAS, 524, 3596
Dillamore, A. M., Monty, S., Belokurov, V., & Evans, N. W. 2024b, ApJL, 971, L4
Di Matteo, P., Haywood, M., Combes, F., Semelin, B., & Snaith, O. N. 2013, A&A, 553, A102
Fragkoudi, F., Di Matteo, P., Haywood, M., et al. 2017, A&A, 606, A47
Frankel, N., Rix, H.-W., Ting, Y.-S., Ness, M., & Hogg, D. W. 2018, ApJ, 865, 96
Frankel, N., Sanders, J., Ting, Y.-S., & Rix, H.-W. 2020, ApJ, 896, 15
Gaia Collaboration, Vallenari, A., Brown, A. G. A., et al. 2023, A&A, 674, A1
Hackshaw, Z., Hawkins, K., Filion, C., et al. 2024, ApJ, 977, 143
Halle, A., Di Matteo, P., Haywood, M., & Combes, F. 2015, A&A, 578, A58
Halle, A., Di Matteo, P., Haywood, M., & Combes, F. 2018, A&A, 616, A86
Hamilton, C., Modak, S., & Tremaine, S. 2024, arXiv:2411.08944
Hawkins, K. 2023, MNRAS, 525, 3318
Hayden, M. R., Bovy, J., Holtzman, J. A., et al. 2015, ApJ, 808, 132
Haywood, M., Khoperskov, S., Cerqui, V., et al. 2024, A&A, 690, A147
Kawata, D., Baba, J., Hunt, J. A. S., et al. 2021, MNRAS, 508, 728
Khoperskov, S., Di Matteo, P., Haywood, M., Gómez, A., & Snaith, O. N. 2020, A&A, 638, A144
Khoperskov, S., Haywood, M., Snaith, O., et al. 2021, MNRAS, 501, 5176
Khoperskov, S., Minchev, I., Libeskind, N., et al. 2023, A&A, 677, A91
Khoperskov, S., Steinmetz, M., Haywood, M., et al. 2024, arXiv:2411.16866
Li, C., Yuan, Z., Monari, G., et al. 2024, A&A, 690, A26
Lian, J., Zasowski, G., Hasselquist, S., et al. 2022a, MNRAS, 511, 5639
Lian, J., Zasowski, G., Mackereth, T., et al. 2022b, MNRAS, 513, 4130
Liao, X., Li, Z.-Y., Simion, I., et al. 2024, ApJ, 967, 5
Libeskind, N. I., Carlesi, E., Grand, R. J. J., et al. 2020, MNRAS, 498, 2968
Lu, Y., Buck, T., Nidever, D., et al. 2024, MNRAS, 532, 411
Lu, Y. L., Minchev, I., Buck, T., et al. 2024, MNRAS, 535, 392
Lu, Y. L., Ness, M. K., Buck, T., & Carr, C. 2022, MNRAS, 512, 4697
McMillan, P. J. 2017, MNRAS, 465, 76
Miglio, A., Chiappini, C., Mackereth, J. T., et al. 2021, A&A, 645, A85
Minchev, I., Anders, F., Recio-Blanco, A., et al. 2018, MNRAS, 481, 1645
Minchev, I., Chiappini, C., & Martig, M. 2013, A&A, 558, A9
Minchev, I., & Famaey, B. 2010, ApJ, 722, 112

Minchev, I., Famaey, B., Combes, F., et al. 2011, A&A, 527, A147

Minchev, I., & Quillen, A. C. 2006, MNRAS, 368, 623

Nelson, D., Springel, V., Pillepich, A., et al. 2019, ComAC, 6, 2

Poggio, E., Recio-Blanco, A., Palicio, P. A., et al. 2022, A&A, 666, L4

Portail, M., Gerhard, O., Wegg, C., & Ness, M. 2017, MNRAS, 465, 1621

Queiroz, A. B. A., Anders, F., Chiappini, C., et al. 2023, A&A, 673, A155

Quillen, A. C., Minchev, I., Bland-Hawthorn, J., & Haywood, M. 2009, MNRAS, 397, 1599

Ratcliffe, B., Khoperskov, S., Minchev, I., et al. 2024a, arXiv:2410.17326

Ratcliffe, B., Khoperskov, S., Minchev, I., et al. 2024b, A&A, 690, A352

Renaud, F., Agertz, O., Andersson, E. P., et al. 2021, MNRAS, 503, 5868

Rix, H.-W., Chandra, V., Andrae, R., et al. 2022, ApJ, 941, 45

Roškar, R., Debattista, V. P., Quinn, T. R., Stinson, G. S., & Wadsley, J. 2008, ApJL, 684, L79

Roškar, R., Debattista, V. P., Quinn, T. R., & Wadsley, J. 2012, MNRAS, 426, 2089

Sanders, J. L., & Binney, J. 2015, MNRAS, 449, 3479

Sanders, J. L., Kawata, D., Matsunaga, N., et al. 2024, MNRAS, 530, 2972

Sanders, J. L., Smith, L., & Evans, N. W. 2019, MNRAS, 488, 4552

Schönrich, R., & Binney, J. 2009, MNRAS, 396, 203

Sellwood, J. A., & Binney, J. 2025, arXiv:2501.17907

Sellwood, J. A., & Binney, J. J. 2002, MNRAS, 336, 785

Semczuk, M., Dehnen, W., Schönrich, R., & Athanassoula, E. 2024, A&A, 692, A159

Sharma, S., Hayden, M. R., & Bland-Hawthorn, J. 2021a, MNRAS, 507, 5882

Sharma, S., Hayden, M. R., Bland-Hawthorn, J., et al. 2021b, MNRAS, 506, 1761

Solway, M., Sellwood, J. A., & Schönrich, R. 2012, MNRAS, 422, 1363

Sormani, M. C., Gerhard, O., Portail, M., Vasiliev, E., & Clarke, J. 2022, MNRAS, 514, L1

Vasiliev, E. 2019, MNRAS, 482, 1525

Virtanen, P., Gommers, R., Oliphant, T. E., et al. 2020, NatMe, 17, 261

Wang, C., Huang, Y., Yuan, H., et al. 2022, ApJS, 259, 51

Wang, L., Dutton, A. A., Stinson, G. S., et al. 2015, MNRAS, 454, 83

Weinberg, M. D., & Katz, N. 2007, MNRAS, 375, 460

Xiang, M., & Rix, H.-W. 2022, Natur, 603, 599

Xiang, M., Ting, Y.-S., Rix, H.-W., et al. 2019, ApJS, 245, 34

Yu, Z., Li, J., Chen, B., et al. 2021, ApJ, 912, 106

Yuan, Z., Li, C., Martin, N. F., et al. 2024, A&A, 691, L1

Zhang, H., Ardern-Arentsen, A., & Belokurov, V. 2024a, MNRAS, 533, 889

Zhang, H., Belokurov, V., Evans, N. W., Kane, S. G., & Sanders, J. L. 2024b, MNRAS, 533, 3395

Zhang, H., Belokurov, V., Evans, N. W., et al. 2024c, MNRAS, 535, 2873

Zhang, H., Chen, Y., & Zhao, G. 2021, ApJ, 919, 52